Geophysical Research Letters

RESEARCH LETTER
10.1029/2018GL081074

Key Points:
- We observe a significant increase of seismicity rate in the last day before the mainshock
- The mainshock ruptured beyond the Tehuantepec Ridge with a fast speed
- The large magnitude is explained by reactivation of large outer-rise normal faulting

Supporting Information:
- Supporting Information S1

Correspondence to:
L. Meng,
meng@ess.ucla.edu

Citation:
Meng, L., Huang, H., Xie, Y., Bao, H., & Dominguez, L. A. (2019). Nucleation and kinematic rupture of the 2017 Mw 8.2 Tehuantepec earthquake. *Geophysical Research Letters*, *46*, 3745–3754. https://doi.org/10.1029/2018GL081074

Received 26 OCT 2018
Accepted 27 MAR 2019
Accepted article online 1 APR 2019
Published online 8 APR 2019

Nucleation and Kinematic Rupture of the 2017 Mw 8.2 Tehuantepec Earthquake

Lingsen Meng[1], Hui Huang[1], Yuqing Xie[1], Han Bao[1], and Luis A. Dominguez[2]

[1]Earth Planetary and Space Sciences, University of California, Los Angeles, CA, USA, [2]National School for Advanced Studies, National Autonomous University of Mexico, Morelia, Mexico

Abstract Integrated observations from the 2017 Mw 8.2 Tehuantepec, Mexico, earthquake probe one of the largest normal-faulting events inside a subducting slab. In this study, we utilize a template matching approach to detect possible missing earthquakes within a 2-month period before the mainshock. The seismicity rate shows an abrupt increase in the last day around the mainshock hypocenter. The large distance between most of the foreshocks and the mainshock is not consistent with static stress triggering but suggests alternative mechanisms such as delayed dynamic triggering or aseismic transients. Back-projection using the USArray network reveals that the rupture propagated northwestward unilaterally at a speed of 3.6 km/s and terminated north of the Tehuantepec Ridge. Towards the end of the rupture, a wide step-over occurred onto an adjacent fault parallel to the main fault plane. The mainshock is likely a reactivation of subducted outer-rise faults, supported by the similarity of fault-strike angles. The surprisingly large magnitude is consistent with exceedingly large dimensions of outer-rise faulting in this segment of the central Mexican trench.

1. Introduction

Determining what is the largest magnitude that a given fault system is able to produce, and what is the role of the so-called seismic gaps is essential for understanding the actual seismic hazard. In this regard, the 8th of September 2017 Tehuantepec earthquake represents a new opportunity to test what are the key factors that determine the occurrence of large intraplate earthquakes on previously relatively quiescent fault systems (Hjörleifsdóttir et al., 2009; Meng, Ampuero, Sladen, etal., 2012; Satriano et al., 2012; Yue et al., 2012). This earthquake is ranked as the strongest intraplate event ever recorded in Mexico with a moment magnitude of M 8.2, and the third largest intraplate event known globally (Wiens et al., 1998; Yue et al., 2012). Unlike most of the major earthquakes that are thrust events occurring along the Middle America trench in Mexico, the 8 September 2017 event had a normal fault mechanism which caused severe damage in the epicentral region, mainly in the states of Oaxaca, Tabasco, and Chiapas. The Mexican earthquake early warning system delivered an alert to major cities in central Mexico within a few seconds after the earthquake, sirens in Mexico City went off 92 s before the arrival of the surface waves which arrived near midnight 7 September 2017 local time (Suárez et al., 2018). Eleven days after the event, another intraslab earthquake ruptured near Mexico City (e.g., Melgar, Pérez-Campos, et al., 2018) causing widespread damage in Mexico's capital, where nearly ~300 people died and ~45 building collapsed due to basin amplification (Çelebi et al., 2018; Cruz-Atienza et al., 2016; Galvis et al., 2017; Sahakian et al., 2018; Singh et al., 2018). This event coincidentally occurred on the 32nd anniversary of the great 1985 M 8.1 Michoacan earthquake, only 2 hr after the annual national earthquake drill. The relationship between the M 8.2 and subsequent M 7.1 has been tested but no triggering mechanism has been discovered at the time of this publication (Segou & Parsons, 2018).

In Mexico, the Middle America trench produces most of the seismic activity along a narrow band near the trench where the Cocos, Rivera, and North America plates converge at a rate of 5.9–6.5 cm/year (DeMets et al., 2010). In the last century, three great earthquakes with magnitudes larger than M 8.0 were instrumentally recorded along the trench in 1932 (M 8.2 Colima Earthquake), 1985 (M 8.1 Michoacán Earthquake), and 1995 (M 8.0 Manzanillo earthquake). Except for the 1902 earthquake whose location and magnitude remain very unclear, all these major events had ruptured the northwestern extent of trench. No great earthquakes had been recorded in the southeast of Mexico until now (Suárez et al., 2019, and reference herein). Nonetheless, historical records and tsunami deposits suggest that a ~M 8.6 earthquake could have ruptured this segment in a single event in 1787 which likely affected the Tehuantepec region (Suárez & Albini, 2009). Hence, this region had remained absent of M > 8 for at least hundreds of years. The Tehuantepec zone forms a triple junction between the Cocos, Caribbean, and North American plates with significant lateral variations. A noteworthy feature, known as the Tehuantepec ridge, subducts almost perpendicular to the trench, which has important implications on tectonics of the area (Manea & Manea, 2008; Ramírez-Herrera et al., 2011). The age of the ocean floor significantly varies across the Tehuantepec rift from roughly ~15 Ma at the northwest side, to ~26 Ma at the Southeast, indicating differential convergence rates at either side of the rift (Manea et al., 2005). Another significant characteristic, of this area, is the abrupt transition from a steep dipping subduction angle of the Cocos plate, toward subhorizontal, flat subduction in Central Mexico from the coast up to ~250 km inland (Pardo & Suárez, 1995; Pérez-Campos et al., 2008; Kim et al., 2010; Melgar & Pérez-Campos, 2011; Stubailo et al., 2012). This change in the dipping angle is arguably responsible for the dominant tensile stress at the outer rise.

Previously, several authors had recognized the Tehuantepec gap as a possible location of the next megathrust earthquake in Mexico (Singh et al., 1981; Nishenko & Singh, 1987; Ponce et al., 1992). Although the 2017 M 8.2 rupture coincides with the segment where the next large earthquake was expected, the rupture itself took place within the Cocos plate and not at the plate interface. Due to the large depth (e.g., Okuwaki & Yagi, 2017; Ye et al., 2017) of the rupture, no significant tsunami was induced, with an average wave height of 1.5 m and a maximum runup of 3 m causing minor damage along coastal areas in Mexico (Chen et al., 2018; Ramírez-Herrera et al., 2018). A resonant wave tide was reported for several hours after the event in some areas of the Tehuantepec bay (Melgar & Ruiz-Angulo, 2018).

The National Seismological Service (SSN) reported a moment magnitude of M 8.2, and an epicenter located at 14.761°N, 94.103°W and 45.9 km depth (SSN, 2017). The kinematic rupture processes of the M 8.2 event are characterized by a unilateral northwestward rupture propagation and a principle slip zone deeper than 25 km (Chen et al., 2018; Melgar, Ruiz-Angulo, et al., 2018; Okuwaki & Yagi, 2017; Ye et al., 2017; Zhang & Brudzinski, 2019). Okuwaki and Yagi (2017) suggested that the rupture terminated at the Tehuantepec Ridge which prevented a larger rupture area. A multiarray back-projection (BP) analysis seems to support that the main branch of the rupture ends before reaching the Tehuantepec Ridge (Zhang & Brudzinski, 2019). Here, we show that the rupture length inferred from conventional BPs is distorted by 3-D path effects. We apply a slowness-enhanced BP (SEBP) approach which calibrates the travel-time errors based on aftershock locations. Compared with previous studies, our improved BP image clearly indicates that the mainshock ruptured beyond the Tehuantepec ridge and a wide step over occurred between two parallel normal faults toward the end of the rupture.

We also report a previously undocumented foreshock sequence prior to the Tehuantepec earthquake. Foreshock sequences were found to be an important manifestation of precursory physical processes (e.g., static stress transfer, slow slip, or other deformation transients) leading up to some recent large interplate earthquakes, for example, the 2011 M 9.0 Tohoku-Oki earthquake (Kato et al., 2012), the 2014 M 8.2 Iquique earthquake (Meng et al., 2015), and the 2015 M 8.3 Illapel earthquake (Huang & Meng, 2018). Bouchon et al. (2013) showed that ~70% of the M > 7 interplate earthquakes were preceded by accelerating foreshock sequences. However, it is still not clear whether foreshock sequences precede intraplate earthquakes, possibly limited by the detection capability of routine methods which may miss events generating signals with low signal-to-noise ratio (SNR). Here, we apply the template matching approach to recover the earthquake sequence that preceded the 2017 M 8.2 Tehuantepec mainshock to better understand the nucleation process before a large intraplate earthquake. The seismicity rate shows an abrupt increase in the last day around the mainshock hypocenter. The focal mechanism and relative relocation suggest that the largest foreshock (M 4.6) occurred on the same fault plane with the Mw 8.2 mainshock. The large distance between most of the foreshocks and the mainshock is not consistent with static stress triggering and suggests alternative mechanisms such as delayed dynamic triggering or aseismic transients.

2. Matched-Filter Detection of Foreshocks

To better characterize the temporal evolution of pre-mainshock events, we apply the matched-filter method to search continuous data in a 70-day period before the M 8.2 mainshock. Three-component seismograms were collected from 1 July through 8 September 2017 at seven nearby stations (Figure S1), which are

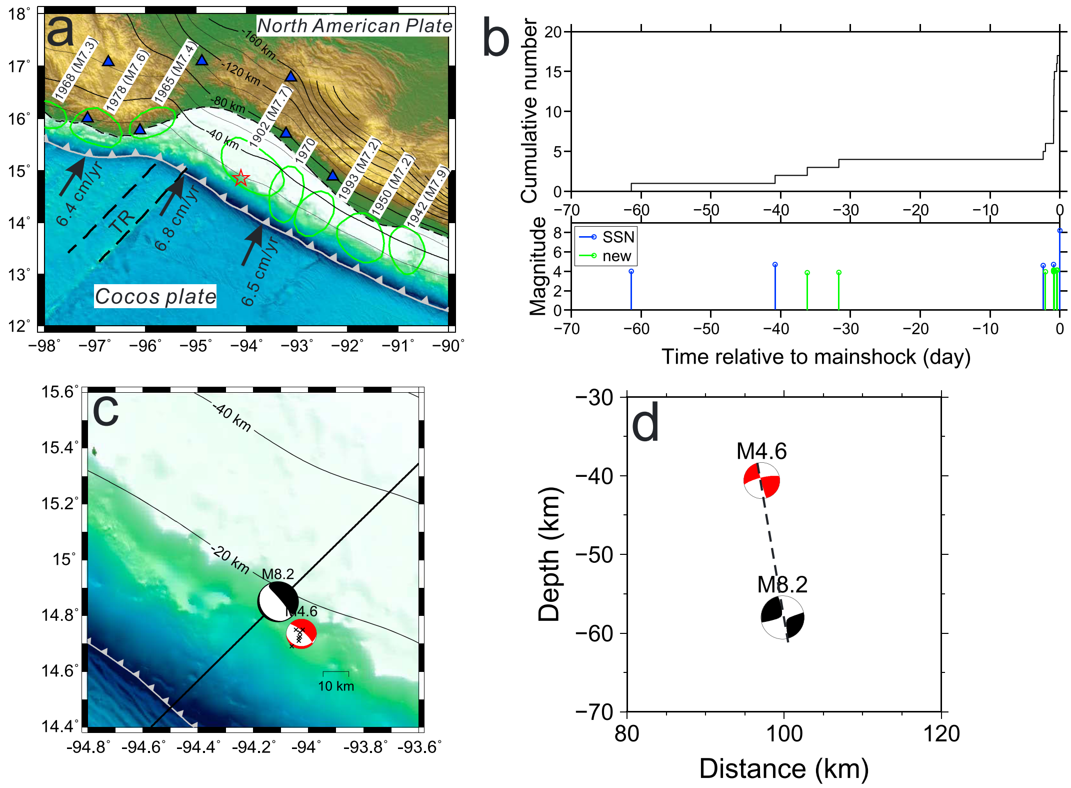

Figure 1. (a) The tectonic background of the subduction zone around the 2017 M 8.2 Tehuantepec earthquake (red star). The blue triangles denote the seven broadband stations used in the matched-filter analysis. The green enclosed areas denote historical M > 7 subduction megathrust earthquakes (Lowry et al., 2001). TR denotes the Tehuantepec Ridge. (b) shows the cumulative number (upper) and magnitudes (lower) of M ≥ 3.7 seismicity (>20 km depth) within 30 km from the M 8.2 epicenter. (c) shows the relocated M 4.6 event relative to the mainshock. The black crosses denote the relocated locations of other seven foreshocks within the last day (see text for details). (d) shows the depth section projected along the black thick line in (c). The dashed line in (d) shows the approximate fault plane for these two earthquakes. SSN = National Seismological Service.

operated by the SSN network (Figure 1a). We use the SSN catalog (98–90°W, 12–18°N) as the template data set, which starts from January 2007 through October 2017. The template waveforms are windowed from 5 s before to 15 s after the theoretical S arrival times. We retain 7,796 templates recorded on a minimum of 12 channels and a high SNR (SNR ≥ 5). We calculate the cross-correlation coefficients (CC) between the templates and the continuous seismograms and average the CC traces over available channels according to the S arrival times at different stations. To define a positive detection, we use a threshold of 10 times the median absolute deviation of the CC in each day. We remove the duplicate detections by defining the new event location to be the location of the template corresponding to the highest CC between the template and data. Then we estimate the magnitude of the detected events based on the relation between the magnitude difference and maximum absolute amplitude ratio determined at each station (Figure S2; Huang & Meng, 2018).

A total of 5,452 new events are detected within 70 days before the mainshock, ~4 times more than the SSN catalog. To investigate the evolution of seismicity rate within the subducting plate, we exclude shallow events (≤20 km depth) from the catalog. We plot the cumulative number of seismicity within 30 km around the M 8.2 epicenter. The magnitude of completeness (Mc) is estimated to be ~3.7 (Figure S3) by applying the maximum curvature method (Wiemer, 2001). It shows that the seismicity rate increases within the last day before the mainshock (Figure 1b). The waveforms of the detected events can be seen at close stations with relatively low SNR (Figure S4). We apply the β statistics to the enhanced catalog to test the significance of seismicity-rate variation (e.g., Matthews & Reasenberg, 1988). A β value greater than 2 is used to infer periods of significant accelerating activities relative to a background time period while a value smaller than −2 indicates significant deceleration. The two time periods are chosen as [-60 -1] and [-1 0] days relative to the mainshock. We find that the β value is ~50 around the epicenter, indicating significant accelerations in seismicity within the last day (Figures S5a and S5b).

Among the foreshock sequence within the last day, 10 new events are detected using a M 4.6 event template. The M 4.6 event is the first and largest event in this foreshock sequence, with enough clear waveforms that we can assess its relative location to the M 8.2 mainshock, as well as the focal mechanism. We perform a grid search in the horizontal plane to relocate the M 4.6 event relative to the M 8.2 mainshock based on the Pn phase arrival data (e.g., Wen, 2006) retrieved from ANSS Comprehensive Earthquake Catalog. The result shows that the M 4.6 event is located at an epicentral distance of ~15.7 km to the southeast of the M 8.2 event (Figure S6). To infer the relative locations of the other 10 foreshocks relative to the M 4.6 event, we measure the Pn differential travel times from cross correlations which are input into the grid search. The result shows that most of the other foreshocks (7 out of 10) are located within 0.7–6.2 km epicentral distance from the M 4.6 event (Figures S7–S8), away from the M 8.2 mainshock (Figure 1c). To estimate the focal mechanism and depth of the M 4.6 event, we apply the Cut-and-Paste focal mechanism inversion method (Zhu & Rivera, 2002) using the seismic waveforms recorded by regional broadband stations (Figure S9). We adopt the 1-D velocity model of Rebollar et al. (1999) to calculate the Green's functions. The optimal nodal planes (strike, dip, rake) are 90°, 19°, −130° and 311.6°, 75.6°, −77.5°, with the latter one consistent with the USGS-NEIC fault-plane solution of the mainshock (314°, 73°, −100°). The optimal focal depth of the M 4.6 event is 40.6 km (Figure S9). Note that the second nodal planes determined by other 1-D velocity models show similar result with slightly lower variance reduction for waveform fitting (Figures S10 and S11). In addition, we also inspect the initial part of the waveforms of the M 4.6 and M 8.2 events, which show high similarity at some stations with different azimuths (Figure S12), supporting the similar focal mechanism of these two events.

3. BP of the Coseismic Rupture Process

BPs highlight the high-frequency aspect of the 2018 Mw 8.2 Tehuantepec earthquake. The technique tracks the seismic wavefield of the earthquake and extracts kinematic spatiotemporal characteristics, such as source dimension, directivity, rupture speed, and fault segmentation (Kiser & Ishii, 2017). The high-frequency radiators inferred by BP are typically regarded as a proxy of the rupture front. One mechanical interpretation is that the high-frequency radiated energy is modulated by the duration of the positive slip acceleration, the shortest time scale of the slip-rate function for spontaneous cracks. This positive slip acceleration is bounded at and near the propagating crack tip (Tinti et al., 2005), therefore the high-frequency radiators approximates the locations of the rupture front. Here, we applied the Multitaper-MUSIC seismic array-processing technique enhanced by the "reference window" strategy, which resolves closely spaced simultaneous sources and eliminates "swimming" artifacts, yielding a sharper and more robust source image than the conventional beamforming approach (Meng et al., 2011; Meng, Ampuero, Stock, et al., 2012). We conduct BP analysis on coherent *P* wave arrivals recorded by the USArray, composed of ~272 broadband stations across Alaska with epicentral distances between 50° and 70° (Figure 2—inset). We band pass filter the seismograms between 0.5 and 2 s, the shortest periods with adequate waveform coherence.

The travel-time variation due to 3-D path effects is a crucial factor affecting the quality of BP images. Standard BPs adopt the travel times inferred from a one-dimensional layered Earth model (e.g., IASP91) and apply the "hypocenter correction," which obtains a set of static travel-time errors by cross-correlating the first P phase arrivals (Ishii et al., 2005). The subsequent rupture propagation is imaged according to the differential travel time relative to the SSN mainshock hypocenter (94.103°W, 14.761°N). However, the hypocenter correction becomes less valid for large earthquakes when the rupture front propagates far from the hypocenter. Here, in addition to the hypocenter correction, we also applied a slowness correction that accounts for the spatial derivatives of the travel times in the source region. The SEBP reduces the spatial bias and improves the consistency between BP using different arrays (Bao et al., 2019; Meng et al., 2016; Meng et al., 2018). The slowness correction term can be inferred using the relocated locations of aftershocks. For a set of aftershocks, their differential travel-times relative to the hypocenter are compared to those predicted by the one-dimensional reference velocity model. The remaining difference of travel-time and the mainshock-aftershock distances are used to solve for the slowness correction terms in a least-squares sense.

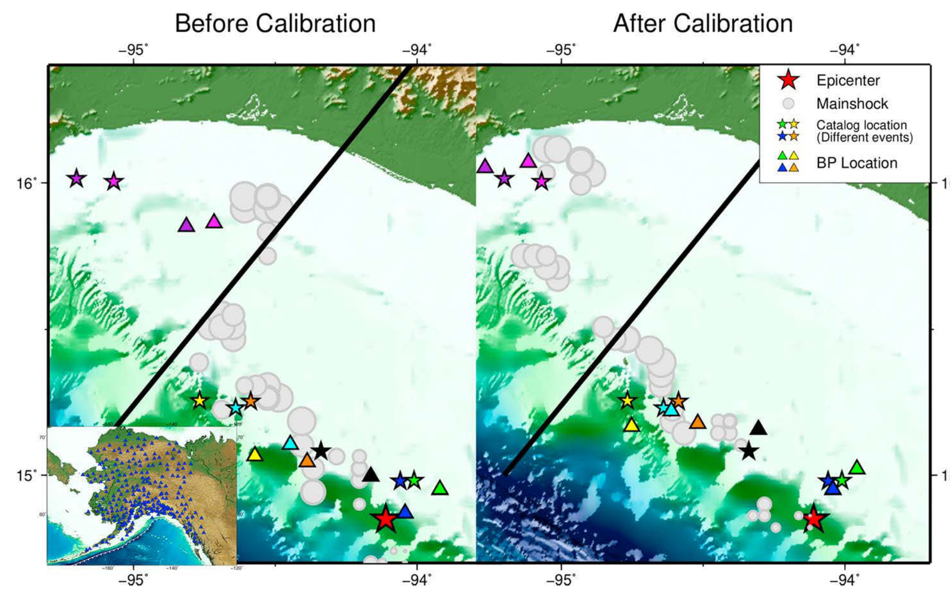

Figure 2. Comparisons of BP-inferred (triangles) and National Seismological Service relocated catalog (stars) locations of 7 M6+ aftershocks surrounding the Tehuantepec mainshock before (left) and after (right) the slowness calibrations. The gray circles are the corresponding mainshock BP sources before and after the calibrations. The background topography and bathymetry is based on ETOPO1.The black solid line is the surface expression of the subducted Tehuantepec Ridge. The inset map on the left panel shows the station distribution of the USArray. BP = back-projection.

For the 2017 M 8.2 Tehuantepec earthquake, we derived the slowness correction terms based on six aftershocks evenly distributed across the mainshock rupture zone (Figure 2). We chose relatively large aftershocks ($M > 6$) so that the initial *P* waves have enough SNR between 0.5 and 2 Hz at teleseismic distances. Here, we adopt the SSN event catalog relocated by a double-difference method with local stations, so that the earthquake location errors are small enough for a reliable slowness calibration (Table S1). Figure 2 compares the BP-imaged aftershock locations with and without the slowness correction with respect to the SSN relocated catalog locations. Without the calibration (Figure 2a), the BP locations are generally biased westward with a root-mean-square error of 29.33 km. With the slowness calibration, these aftershocks are significantly closer to their catalog locations and the root-mean-square error is reduced to 8.11 km (Figure 2b).

We then perform the MUSIC BP enhanced by this slowness correction to the Tehuantepec mainshock. Figure 3a illustrates the spatiotemporal characteristics of short-period sources during the rupture process. The SEBP identifies coherent sources for approximately 60 s after the rupture initiation. The HF sources follow a remarkably linear rupture path toward the NNW in the first 30 s. The slowness calibration systematically shifts the BP locations toward the NW direction, which is consistent with the pattern of aftershock calibrations (Figure 2). This shift has an overall effect producing a longer rupture length and higher rupture speed (Figure 2). The length and overall rupture speed of the first mainshock branch increased from 120 km and 2.9 km/s before the calibration to 150 km and 3.6 km/s after the slowness calibration (Figure 3b). Without the calibration, the first part of the mainshock rupture appears to end near the Tehuantepec ridge similar to that imaged by conventional BP (Zhang & Brudzinski, 2019). With the slowness calibration, the SEBP clearly indicates the rupture went beyond the Tehuantepec ridge at approximately 30 s after the initiation. The longer rupture length inferred from SEBP is more consistent with the rupture zone manifested by dense aftershock distributions (Figure 3a). At about 50 s, we observe a jump of HF sources toward the northeast direction, seemingly onto an adjacent fault parallel to the initial fault plane. Both the initial and second fault traces are evident from the aftershock pattern. This secondary HF source is also present in the conventional BP (Zhang & Brudzinski, 2019). At this stage, the rupture on the second fault generates strong HF radiations comparable to the peak HF power at 30 s when the rupture crosses the Tehuantepec ridge (Figure 3c).

10.1029/2018GL081074

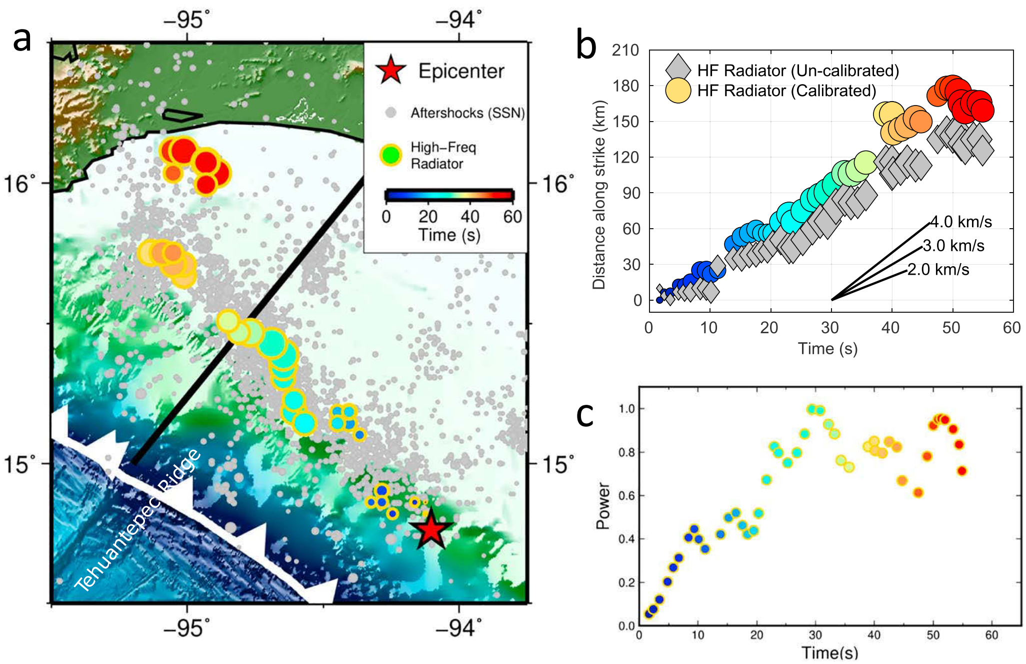

Figure 3. (a) High-frequency back-projection rupture imaging. The colored circles denote peak locations of the back-projection (0.5–2 Hz) in the first 60 s of the mainshock. The circles are sized by the corresponding relative beamforming power and colored by its relative timing with respect to the origin time. The red star denotes the SSN hypocenter. The gray dots denote the relocated aftershocks. The black solid line is the surface expression of the subducted Tehuantepec Ridge. (b) Rupture time versus distance. The timing of the high frequency radiators seen by the U.S. network are plotted against their distance with respect to the hypocenter before (gray diamonds) and after (colored circles) the slowness calibration. The slope of the black lines indicates rupture speeds of 2.5, 3, and 4 km/s. For reference, the *S* wave velocity at the depth 50 km is 4.12 km/s according to the PREM model. (c) The temporal evolution of normalized amplitudes of HF sources colored coded by time. SSN = National Seismological Service.

One concern of the last step over phase is the perturbation due to the depth phase pP. Since BPs only assume the direct phase, it is possible that strong depth phases may result in northward artifacts toward the array to be misinterpreted as true earthquake sources. We test the effect of the depth phase by inspecting the USArray waveforms and the BP of the small M5.5 earthquake that occurred on 14 October 2017, which has a similar focal depth and focal mechanism as the mainshock. The USArray waveforms show that the smaller earthquake has a noticeable but weak pP phase that arrives ~18 s after the direct P (Figure S13). The BP image indicates the depth phase produces a minor northward artificial source with BP power approximately 20% of the direct P phase (Figures S14 and S15). In the case of the mainshock the last subevent on the second fault has a strong and comparable source amplitude with the peak power. Therefore, we consider the last subevent is likely a true earthquake source instead of an artifact produced by the depth phase pP.

4. Discussion

Previous studies found accelerating foreshock sequences before large megathrust earthquakes, for example, the 2011 M 9.0 Tohoku-Oki earthquake (Kato et al., 2012) and the 2014 M 8.2 Iquique earthquake (Meng et al., 2015). A statistical study shows that the precursory acceleration phase is not found within 50 km around 31 large intraplate earthquakes in the North Pacific (Bouchon et al., 2013). Our observations provide an example of foreshock sequences of a large intraplate earthquake. Our enhanced earthquake catalog reveals a foreshock sequence in the last day located within 30 km of the 2017 M 8.2 Tehuantepec earthquake. The largest M 4.6 event in this sequence is located along the same fault plane and updip from the Tehuantepec mainshock. The β statistic shows that this foreshock sequence results in significant acceleration in seismicity, which appears to be only observed around the Tehuantepec epicenter. These observations support the interpretation that the foreshock sequence is related to the mainshock occurrence.

10.1029/2018GL081074

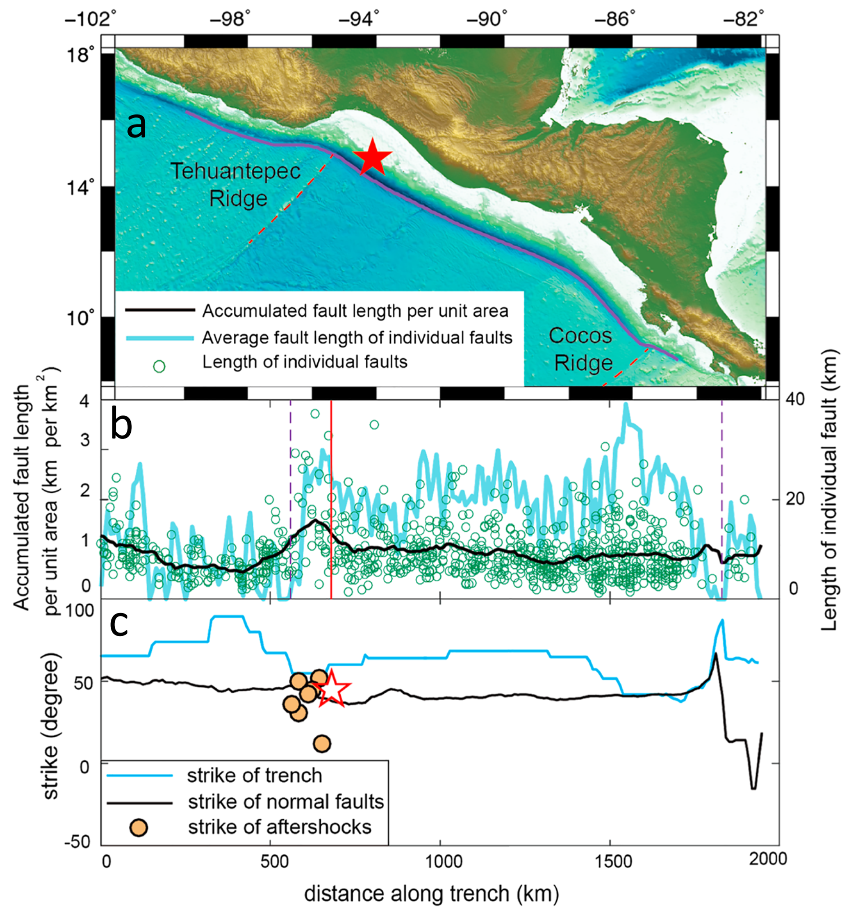

Figure 4. (a) ETOPO1 bathymetry of the Central America trench around the Tehuantepec earthquake. (b) Statistics of the surface fault traces on the outer rise within 35 km from the trench. The black and blue lines and the green circles represent the accumulated fault length per unit area, average fault length per unit area, and the length of individual faults, respectively. (c) Comparison of the strike of the Tehuantepec earthquake sequence, the trench and the outer-rise normal faults. The aftershocks are chosen with rake angle larger than 0, magnitude larger than 5, and depths larger than 20 km from 8 July 2017 to 24 September 2017.

The stress triggering relation between the foreshock sequence and the mainshock is usually attributed to static stress triggering, dynamic triggering, or aseismic transients such as slow slip or fluid flow. The source radius of the M 4.6 event (largest event in the foreshock sequence) is ~1.1 km assuming a stress drop of 3 MPa, significantly smaller than its hypocentral distance of 23.4 km (horizontal and vertical offset of ~15.7 and 17.4 km, respectively) to the M 8.2 mainshock. The static stress change induced by fault rupture drops significantly with distance and becomes negligible when the receiver fault is located over two times the rupture length away (Hill & Prejean, 2007). Thus, it is unlikely that the M 8.2 rupture is triggered by static stress transfer induced by the M 4.6 foreshock. Most of the other smaller foreshocks are also inferred to be farther away from the M 8.2 hypocenter (Figure 1c), imparting little static stress transfer to the mainshock. We note that static stress triggering by possible small events that are undetected due to the limited station coverage cannot be ruled out. However, the dynamic stress change induced by the M 4.6 event is estimated to be ~71 KPa at the M 8.2 hypocenter (Van Der Elst & Brodsky, 2010). This value is larger than the typical triggering threshold of ~10 KPa observed in other tectonic settings (Brodsky & Prejean, 2005). Therefore, the dynamic stress change is one possible interpretation of the triggering relation between the foreshock sequence and the mainshock. Alternatively, slow slip along the fault plane may also be responsible for both the foreshock sequence and the mainshock, although any migration of the foreshock sequence is not resolved by our observations.

The pattern of the HF radiation revealed by BP analysis provides a remarkable opportunity to understand the mechanisms of this mega-normal earthquake. The overall rupture speed appears fast at 3.6 km/s. However, considering the source focal depth of 50 km, the rupture speed is about 85% of the ambient shear-wave speed and 92% of the Rayleigh-wave speed (based on the PREM model), which are within the normal range of subshear rupture speed for the propagating mode III crack. Another important observation is that the rupture propagates beyond the Tehuantepec ridge as is evident based on both the coseismic BP radiators and the lineation of the aftershock distribution. It is worth noting that there is no apparent slowdown in rupture speed and the beamforming power reaches its maximum around the time when rupture crosses the ridge. This indicates that the subducting ridge did not act as a geometrical barrier in this particular earthquake. The Tehuantepec earthquake also features a wide step over between two parallel normal faults toward the end of the rupture. Considering the typical continental step overs are less than 5 km (Wesnousky, 2005), this 40 km gap between two rupture branches is extremely large. One possible explanation is that the wide step over is facilitated by the large seismic width of the intraplate normal faulting. The area of influence of the coseismic stress field (both dynamic and static) are proportional to the seismogenic depth. Given similar settings of initial stresses, the maximum crossover distance are greater for larger seismogenic depth, since their stress fields have a further reach (Bai & Ampuero, 2017). In the case of the Tehuantepec earthquake, several finite fault studies suggest that the principal slip zone extends over a depth range of 25 km (USGS finite fault model; Ye et al., 2017; Okuwaki & Yagi, 2017; Chen et al., 2018; Melgar, Ruiz-Angulo, et al., 2018). Such source width is considerably larger than the typical crustal seismogenic width of ~10 km in continental settings. This large seismogenic width may facilitate wide step over and is likely associated with the reactivation of the preexisting bending-related faults which are further weakened by the mantle serpentinization through the subduction process (Ranero et al., 2003).

The reactivation of the outer-rise faulting also explains the excessive large magnitude of this particular normal-faulting event. Previous studies found that south of the Cocos plate the intermediate-depth earthquakes are consistent with outer-rise faults in strike orientations (Ranero et al., 2005). We survey the surface fault traces of the outer-rise faulting manifested by the bathymetry fabrics in Central America (Figure 4a). We adopt the 15-arc-seconds SRTM15_plus bathymetry data (Olson et al., 2014). The fault traces are manually picked as the linear features with maximum gradient contrast on the bathymetry map. Examples of normal-fault traces are shown in Figure S16b. We compute both the average fault length and fault density (accumulated fault length per area) by analyzing the faults in a moving 16 by 16 km square window along a survey line parallel to the trench (Figure S16b). We calculate the fault density in addition to the average fault length to account for the fact that a single deep fault might branch out into several smaller surface traces. We find that not only are the strikes of the outer-rise faults consistent with the Tehuantepec earthquakes and its aftershocks (Figure 4c), the fault density reaches its peak around the location of the Tehuantepec earthquake (Figure 4b) and is significantly larger than those at other locations in central America and northern south American margins (Figures S16b and S16e). This evidence indicates that the preexisting bending-related faults in this area have particularly large dimensions which promote large intraplate normal events.

5. Conclusion

In this paper, we present the key observations describing the nucleation and coseismic rupture process of the 2017 Mw 8.2 Tehuantepec Earthquake, one of the largest ever recorded normal faulting events inside a subducting slab. We found a precursory foreshock sequence (largest event M 4.6) in the last day leading up to the mainshock. The largest M 4.6 foreshock occurs on the same fault plane located 23.4 km to the southeast and updip from the mainshock hypocenter. Most of the foreshocks are too distant from the mainshock to promote static stress triggering, indicating that other mechanisms such as dynamic triggering or aseismic transients are involved. Our improved BP imaging also reveals the geometrical particularity of the Tehuantepec mainshock. The mainshock ruptured beyond the Tehuantepec Ridge with fast rupture speed of 3.6 km/s approaching 85% of the local shear wave speed. A wide step over of over 40 km occurs at the end of the rupture, likely benefiting from large seismogenic width. The mainshock is likely a reactivation of subducted outer-rise faults, supported by the similarity of the strike angle between the mainshock and the outer-rise faults. The surprisingly large magnitude is consistent with the exceedingly large dimensions of outer-rise faulting in this particular segment of the central Mexican trench.

Acknowledgments
This research was supported by National Science Foundation Earthscope EAR-1614609 and National Science Foundation Geophysics EAR-1723192, by UC Mexus project #20173956, by the Leon and Joanne V. C. Knopoff Fund, and by the 2017 UCLA Big Data Initiative. The IRIS (www.iris.edu) data centers provided access to broadband seismograms of U. S. network. The earthquake catalogs are obtained from National Earthquake Information Center (NEIC; http://earthquake.usgs.gov/) and México Servicio Sismológico Nacional (SSN; http://www.ssn.unam.mx/). SSN data were obtained by the Servicio Sismológico Nacional (México), station maintenance, data acquisition and distribution is thanks to its personnel. The continuous data of the local broadband stations are provided by the National Autonomous University of Mexico (UNAM). The background topography and bathymetry used in our figures are provided by the National Centers for Environmental Information of NOAA (https://www.ngdc.noaa.gov/mgg/global/etopo1sources.html). The authors are also grateful for two anonymous reviewers for their evaluations of the paper.

References

Bai, K., & Ampuero, J. P. (2017). Effect of seismogenic depth and background stress on physical limits of earthquake rupture across fault step overs. *Journal of Geophysical Research: Solid Earth*, *122*, 10280–10298. https://doi.org/10.1002/2017JB014848

Bao, H., Ampuero, J. P., Meng, L., Fielding, E. J., Liang, C., Feng, T., & Huang, H. (2019). Early and persistent supershear rupture of the 2018 Mw 7.5 Palu earthquake. *Nature Geoscience*, *12*, 200–205. https://doi.org/10.1038/s41561-018-0297-z

Bouchon, M., Durand, V., Marsan, D., Karabulut, H., & Schmittbuhl, J. (2013). The long precursory phase of most large interplate earthquakes. *Nature Geoscience*, *6*(4), 299–302. https://doi.org/10.1038/ngeo1770

Brodsky, E. E., & Prejean, S. G. (2005). New constraints on mechanisms of remotely triggered seismicity at Long Valley Caldera. *Journal of Geophysical Research*, *110*, B04302. https://doi.org/10.1029/2004JB003211

Çelebi, M., Sahakian, V. J., Melgar, D., & Quintanar, L. (2018). The 19 September 2017 M 7.1 Puebla-Morelos earthquake: Spectral ratios confirm Mexico City zoning. *Bulletin of the Seismological Society of America*, *108*(6), 3289–3299.

Chen, K., Feng, W., Liu, Z., & Tony Song, Y. (2018). 2017 M w 8.1 Tehuantepec earthquake: Deep slip and rupture directivity enhance ground shaking but weaken the tsunami. *Seismological Research Letters*, *89*(4), 1314–1322. https://doi.org/10.1785/0220170277

Cruz-Atienza, V. M., Tago, J., Sanabria-Gómez, J. D., Chaljub, E., Etienne, V., Virieux, J., & Quintanar, L. (2016 Dec 9). Long duration of ground motion in the paradigmatic valley of Mexico. *Scientific Reports*, *6*, 38807. https://doi.org/10.1038/srep38807

DeMets, C., Gordon, R. G., & Argus, D. F. (2010). Geologically current plate motions. *Geophysical Journal International*, *181*(1), 1–80. https://doi.org/10.1111/j.1365-246X.2009.04491.x

Galvis, F., Miranda, E., Heresi, P., Dávalos, H., & Silos, J. R. (2017). Preliminary statistics of collapsed buildings in Mexico City in the September 19, 2017 Puebla-Morelos earthquake. Technical Report.

Hill, D. P., & Prejean, S. G. (2007). Dynamic triggering. *Treatise on Geophysics*, *4*, 257–291. https://doi.org/10.1016/B978-044452748-6/00070-5

Hjörleifsdóttir, V., Kanamori, H., & Tromp, J. (2009). Modeling 3-D wave propagation and finite slip for the 1998 Balleny Islands earthquake. *Journal of Geophysical Research*, *114*, B03301. https://doi.org/10.1029/2008JB005975

Huang, H., & Meng, L. (2018). Slow unlocking processes preceding the 2015 Mw 8.4 Illapel, Chile, earthquake. *Geophysical Research Letters*, *45*, 3914–3922. https://doi.org/10.1029/2018GL077060

Ishii, M., Shearer, P. M., Houston, H., & Vidale, J. E. (2005). Extent, duration and speed of the 2004 Sumatra–Andaman earthquake imaged by the Hi-Net array. *Nature*, *435*(7044), 933–936. https://doi.org/10.1038/nature03675

Kato, A., Obara, K., Igarashi, T., Tsuruoka, H., Nakagawa, S., & Hirata, N. (2012). Propagation of slow slip leading up to the 2011 Mw 9.0 Tohoku-Oki earthquake. *Science*, *335*(6069), 705–708. https://doi.org/10.1126/science.1215141

Kim, Y., Clayton, R. W., & Jackson, J. M. (2010). Geometry and seismic properties of the subducting Cocos plate in central Mexico. *Journal of Geophysical Research*, *115*, B06310. https://doi.org/10.1029/2009JB006942

Kiser, E., & Ishii, M. (2017). Back-projection imaging of earthquakes. *Annual Review of Earth and Planetary Sciences*, *45*(1), 271–299. https://doi.org/10.1146/annurev-earth-063016-015801

Lowry, A. R., Larson, K. M., Kostoglodov, V., & Bilham, R. (2001). Transient fault slip in Guerrero, southern Mexico. *Geophysical Research Letters*, *28*(19), 3753–3756. https://doi.org/10.1029/2001GL013238

Manea, M., & Manea, V. C. (2008). On the origin of El Chichón volcano and subduction of Tehuantepec Ridge: A geodynamical perspective. *Journal of Volcanology and Geothermal Research*, *175*(4), 459–471. https://doi.org/10.1016/j.jvolgeores.2008.02.028

Manea, M., Manea, V. C., Ferrari, L., Kostoglodov, V., & Bandy, W. L. (2005). Tectonic evolution of the Tehuantepec Ridge. *Earth and Planetary Science Letters*, *238*(1-2), 64–77. https://doi.org/10.1016/j.epsl.2005.06.060

Matthews, M. V., & Reasenberg, P. A. (1988). Statistical methods for investigating quiescence and other temporal seismicity patterns. *Pure and Applied Geophysics*, *126*(2–4), 357–372. https://doi.org/10.1007/BF00879003

Melgar, D., & Pérez-Campos, X. (2011). Imaging the Moho and subducted oceanic crust at the Isthmus of Tehuantepec, Mexico, from receiver functions. *Pure and Applied Geophysics*, *168*(8–9), 1449–1460. https://doi.org/10.1007/s00024-010-0199-5

Melgar, D., Pérez-Campos, X., Ramirez-Guzman, L., Spica, Z., Espíndola, V. H., Hammond, W. C., & Cabral-Cano, E. (2018). Bend faulting at the edge of a flat slab: The 2017 Mw7. 1 Puebla-Morelos, Mexico earthquake. *Geophysical Research Letters*, *45*, 2633–2641. https://doi.org/10.1002/2017GL076895

Melgar, D., & Ruiz-Angulo, A. (2018). Long-lived tsunami edge waves and shelf resonance from the M8. 2 Tehuantepec earthquake. *Geophysical Research Letters*, *45*, 12–414. https://doi.org/10.1029/2018GL080823

Melgar, D., Ruiz-Angulo, A., Garcia, E. S., Manea, M., Manea, V. C., Xu, X., et al. (2018). Deep embrittlement and complete rupture of the lithosphere during the M w 8.2 Tehuantepec earthquake. *Nature Geoscience*, *11*(12), 955–960. https://doi.org/10.1038/s41561-018-0229-y

Meng, L., Ampuero, J.-P., Sladen, A., & Rendon, H. (2012). High-resolution backprojection at regional distance: Application to the Haiti M7.0 earthquake and comparisons with finite source studies. *Journal of Geophysical Research*, *117*, B04313. https://doi.org/10.1029/2011JB008702

Meng, L., Ampuero, J. P., Stock, J., Duputel, Z., Luo, Y., & Tsai, V. C. (2012). Earthquake in a maze: Compressional rupture branching during the 2012 Mw 8.6 Sumatra earthquake. *Science*, *337*(6095), 724–726. https://doi.org/10.1126/science.1224030

Meng, L., Bao, H., Huang, H., Zhang, A., Bloore, A., & Liu, Z. (2018). Double pincer movement: Encircling rupture splitting during the 2015 Mw 8.3 Illapel earthquake. *Earth and Planetary Science Letters*, *495*, 164–173. https://doi.org/10.1016/j.epsl.2018.04.057

Meng, L., Huang, H., Bürgmann, R., Ampuero, J. P., & Strader, A. (2015). Dual megathrust slip behaviors of the 2014 Iquique earthquake sequence. *Earth and Planetary Science Letters*, *411*, 177–187. https://doi.org/10.1016/j.epsl.2014.11.041

Meng, L., Inbal, A., & Ampuero, J.-P. (2011). A window into the complexity of the dynamic rupture of the 2011 Mw 9 Tohoku-Oki earthquake. *Geophysical Research Letters*, *38*, L00G07. https://doi.org/10.1029/2011GL048118

Meng, L., Zhang, A., & Yagi, Y. (2016). Improving back projection imaging with a novel physics-based aftershock calibration approach: A case study of the 2015 Gorkha earthquake. *Geophysical Research Letters*, *43*, 628–636. https://doi.org/10.1002/2015GL067034

Nishenko, S. P., & Singh, S. K. (1987). Conditional probabilities for the recurrence of large and great interplate earthquakes along the Mexican subduction zone. *Bulletin of the Seismological Society of America*, *77*(6), 2095–2114.

Olson, C. J., Becker, J. J., & Sandwell, D. T. (2014, December). A new global bathymetry map at 15 arcsecond resolution for resolving seafloor fabric: SRTM15_PLUS. In AGU Fall Meeting Abstracts.

Okuwaki, R., & Yagi, Y. (2017). Rupture process during the Mw 8.1 2017 Chiapas Mexico earthquake: Shallow intraplate normal faulting by slab bending. *Geophysical Research Letters*, *44*, 11816–11823. https://doi.org/10.1002/2017GL075956

Pardo, M., & Suárez, G. (1995). Shape of the subducted Rivera and Cocos plates in southern Mexico: Seismic and tectonic implications. *Journal of Geophysical Research*, *100*(B7), 12357–12373. https://doi.org/10.1029/95JB00919

Pérez-Campos, X., Kim, Y., Husker, A., Davis, P. M., Clayton, R. W., Iglesias, A., et al. (2008). Horizontal subduction and truncation of the Cocos plate beneath central Mexico. *Geophysical Research Letters*, *35*, L18303. https://doi.org/10.1029/2008GL035127

Ponce, L., Gaulon, R., Suárez, G., & Lomas, E. (1992). Geometry and state of stress of the downgoing Cocos plate in the Isthmus of Tehuantepec, Mexico. *Geophysical Research Letters*, *19*(8), 773–776. https://doi.org/10.1029/92GL00437

Ramírez-Herrera, M. T., Corona, N., Ruiz-Angulo, A., Melgar, D., & Zavala-Hidalgo, J. (2018). The 8 September 2017 Tsunami Triggered by the M_w 8.2 Intraplate Earthquake, Chiapas, Mexico. *Pure and Applied Geophysics*, *175*, 25–34. https://doi.org/10.1007/s00024-017-1765-x

Ramírez-Herrera, M. T., Kostoglodov, V., & Urrutia-Fucugauchi, J. (2011). Overview of recent coastal tectonic deformation in the Mexican subduction zone. *Pure and Applied Geophysics*, *168*, 1415–1433. https://doi.org/10.1007/s00024-010-0205-y

Ranero, C. R., Morgan, J. P., McIntosh, K., & Reichert, C. (2003). Bending-related faulting and mantle serpentinization at the middle America trench. *Nature*, *425*(6956), 367–373. https://doi.org/10.1038/nature01961

Ranero, C. R., Villaseñor, A., Phipps Morgan, J., & Weinrebe, W. (2005). Relationship between bend-faulting at trenches and intermediate-depth seismicity. *Geochemistry, Geophysics, Geosystems*, *6*, Q12002. https://doi.org/10.1029/2005GC000997

Rebollar, C. J., Quintanar, L., Yamamoto, J., & Uribe, A. (1999). Source process of the Chiapas, Mexico, intermediate-depth earthquake (Mw= 7.2) of 21 October 1995. *Bulletin of the Seismological Society of America*, *89*(2), 348–358.

Sahakian, V. J., Melgar, D., Quintanar, L., Ramírez-Guzmán, L., Pérez-Campos, X., & Baltay, A. (2018). Ground Motions from the 7 and 19 September 2017 Tehuantepec and Puebla-Morelos, Mexico, earthquakes. *Bulletin of the Seismological Society of America*. https://doi.org/10.1785/0120180108

Satriano, C., Kiraly, E., Bernard, P., & Vilotte, J.-P. (2012). The 2012 Mw 8.6 Sumatra earthquake: Evidence of westward sequential seismic ruptures associated to the reactivation of a N-S ocean fabric. *Geophysical Research Letters*, *39*, L15302. https://doi.org/10.1029/2012GL052387

Segou, M., & Parsons, T. (2018). Testing earthquake links in Mexico from 1978 up to the 2017 M=8.1 Chiapas and M=7.1 Puebla shocks. *Geophysical Research Letters*, *45*, 708–714. https://doi.org/10.1002/2017GL076237

Singh, S. K., Astiz, L., & Havskov, J. (1981). Seismic gaps and recurrence periods of large earthquakes along the Mexican subduction zone: A reexamination. *Bulletin of the Seismological Society of America*, *71*(3), 827–843.

Singh, S. K., Reinoso, E., Arroyo, D., Ordaz, M., Cruz-Atienza, V., Pérez-Campos, X., et al. (2018). Deadly Intraslab Mexico earthquake of 19 September 2017 (Mw 7.1): Ground motion and damage pattern in Mexico City. *Seismological Research Letters*, *89*, 2193–2203. https://doi.org/10.1785/0220180159

SSN (2017). *Servicio Sismológico Nacional, Instituto de Geofísica*. México: Universidad Nacional Autónoma de México. http://www.ssn.unam.mx, https://doi.org/10.21766/SSNMX/SN/MX

Stubailo, I., Beghein, C., & Davis, P. M. (2012). Structure and anisotropy of the Mexico subduction zone based on Rayleigh-wave analysis and implications for the geometry of the trans-Mexican Volcanic Belt. *Journal of Geophysical Research*, *117*, B05303. https://doi.org/10.1029/2011JB008631

Suárez, G., & Albini, P. (2009). Evidence for great tsunamigenic earthquakes (M 8.6) along the Mexican subduction zone. *Bulletin of the Seismological Society of America*, *99*(2A), 892–896. https://doi.org/10.1785/0120080201

Suárez, G., Espinosa-Aranda, J. M., Cuéllar, A., Ibarrola, G., García, A., Zavala, M., et al. (2018). A dedicated seismic early warning network: The Mexican Seismic Alert System (SASMEX). *Seismological Research Letters*, *89*(2A), 382–391. https://doi.org/10.1785/0220170184

Suárez, G., Santoyo, M. A., Hjorleifsdottir, V., Iglesias, A., Villafuerte, C., & Cruz-Atienza, V. M. (2019). Large scale lithospheric detachment of the downgoing Cocos plate: The 8 September 2017 earthquake (Mw 8.2). *Earth and Planetary Science Letters*, *509*, 9–14. https://doi.org/10.1016/j.epsl.2018.12.018

Tinti, E., Fukuyama, E., Piatanesi, A., & Cocco, M. (2005). A kinematic source-time function compatible with earthquake dynamics. *Bulletin of the Seismological Society of America*, *95*(4), 1211–1223. https://doi.org/10.1785/0120040177

Van Der Elst, N. J., & Brodsky, E. E. (2010). Connecting near-field and far-field earthquake triggering to dynamic strain. *Journal of Geophysical Research*, *115*, B07311. https://doi.org/10.1029/2009JB006681

Wen, L. (2006). Localized temporal change of the Earth's inner core boundary. *Science*, *314*(5801), 967–970. https://doi.org/10.1126/science.1131692

Wesnousky, S. G. (2005). The San Andreas and Walker Lane fault systems, western North America: Transpression, transtension, cumulative slip and the structural evolution of a major transform plate boundary. *Journal of Structural Geology*, *27*(8), 1505–1512. https://doi.org/10.1016/j.jsg.2005.01.015

Wiemer, S. (2001). A software package to analyze seismicity: ZMAP. *Seismological Research Letters*, *72*(3), 373–382. https://doi.org/10.1785/gssrl.72.3.373

Wiens, D. A., Wysession, M. E., & Lawver, L. (1998). Recent oceanic intraplate earthquake in Balleny Sea was largest ever detected. *Eos, Transactions American Geophysical Union*, *79*(30), 353–354. https://doi.org/10.1029/98EO00265

Ye, L., Lay, T., Bai, Y., Cheung, K. F., & Kanamori, H. (2017). The 2017 Mw 8.2 Chiapas, Mexico, earthquake: Energetic slab detachment. *Geophysical Research Letters*, *44*, 11824–11832. http://doi.org/10.1002/2017GL076085

Yue, H., Lay, T., & Koper, K. D. (2012). En échelon and orthogonal fault ruptures of the 11 April 2012 great intraplate earthquakes. *Nature*, *490*(7419), 245–249. https://doi.org/10.1038/nature11492

Zhang, H., & Brudzinski, M. R. (2019). Evidence for rupture through a double Benioff zone during the 2017Mw8.2 Chiapas, Mexico earthquake. *Geophysical Research Letters*, *46*, 652–660. https://doi.org/10.1029/2018GL080009

Zhu, L., & Rivera, L. A. (2002). A note on the dynamic and static displacements from a point source in multilayered media. *Geophysical Journal International*, *148*(3), 619–627. https://doi.org/10.1046/j.1365-246X.2002.01610.x